



## Spatial dispersion in silicon

Subiao Bian 

*Departament de Física Aplicada, Plat Group, IN2UB, Universitat de Barcelona, Barcelona 08028, Spain  
and Institute of Manufacturing Engineering, Huaqiao University, Xiamen 361021, China*

Razvigor Ossikovski 

*LPICM, CNRS, Ecole Polytechnique, Institut Polytechnique de Paris, 91128 Palaiseau, France*

Adolf Canillas 

*Departament de Física Aplicada, Plat Group, IN2UB, Universitat de Barcelona, Barcelona 08028, Spain*

Gerald Jellison 

*Materials Science and Technology Division, Oak Ridge National Laboratory, Oak Ridge, Tennessee 37831, USA*

Oriol Arteaga \*

*Departament de Física Aplicada, Plat Group, IN2UB, Universitat de Barcelona, Barcelona 08028, Spain*



(Received 20 October 2023; revised 29 November 2023; accepted 29 November 2023; published 3 January 2024)

Spatial dispersion (SD) is a nonlocal effect that can introduce optical anisotropy in an otherwise isotropic material, causing the electromagnetic response at a given point to depend not only on the local field, but also on the field in the vicinity of that point. In this study, we investigate the impact of SD on a cubic semiconductorlike silicon, which is typically considered a negligible effect due to the small size of the lattice parameters with respect to the wavelength of light. However, our findings demonstrate that SD can be significant above the band gap, where transmission measurements are not feasible and reflection measurements are required for characterization. We utilize Mueller matrix ellipsometry spectroscopy to quantify the anisotropy caused by SD in (110) and (100) silicon wafers, and determine the complete permittivity tensor of silicon when spatial dispersion is included. In the most general case, this tensor is found to depend on two complex parameters.

DOI: [10.1103/PhysRevB.109.035201](https://doi.org/10.1103/PhysRevB.109.035201)

### I. INTRODUCTION

Spatial dispersion (SD) refers to the dependence of the dielectric properties on the wave vector at a fixed frequency. In essence, this means that the electromagnetic response of a medium depends not only on the wavelength, but also on the direction in which the wave propagates in the medium, even in materials that by crystal symmetry are expected to have an isotropic optical response [1].

The dielectric permittivity tensor  $\varepsilon_{ij}(\omega, \mathbf{k})$  depending on both temporal frequency  $\omega$  and wave vector  $\mathbf{k}$  can be expanded in powers of  $\mathbf{k}$ . This physically means that the displacement current at a certain point depends not only on the electric field at that same point, but also on the electric field in an infinitesimal area surrounding the considered point. In most cases, only the first three terms of the expansion are written,

$$\varepsilon_{ij}(\mathbf{k}) = \varepsilon_{ij} + i\gamma_{ijl}k_l + \alpha_{ijkl}k_lk_m, \quad (1)$$

where repeating subscripts denote summation. The temporal frequency dependence has been omitted to simplify the notation, but it affects all terms of the expansion. The first term

in Eq. (1) corresponds to the permittivity tensor in the absence of SD, which reduces to a scalar for cubic crystals, indicating isotropic optical properties that are independent of the direction of propagation and polarization of light. The tensors  $\gamma_{ijl}$  and  $\alpha_{ijkl}$  are third- and fourth-rank tensors, respectively, and  $k_l$  and  $k_m$  are the components of the wave vector  $\mathbf{k}$ . The second term in Eq. (1) is linear with the wave vector and vanishes in media with inversion symmetry. This phenomenon, known as optical activity or gyrotropy, results in circular anisotropy in the medium, where absorption and refraction differ for left and right circular polarizations [2]. The third term, quadratic with the wave vector, is the one commonly associated with spatial dispersion and can be present in all crystalline classes, including centrosymmetric ones [3]. Optical activity scales as  $a/\lambda$ , where  $a$  is the lattice constant or molecular dimensions, and  $\lambda$  is the wavelength. Natural materials typically exhibit small optical activity values as  $a/\lambda \sim 10^{-3}$ . Therefore, SD scales as  $a/\lambda \sim 10^{-6}$  and is usually considered to be negligible for natural materials [1]. However, as demonstrated in this work, anisotropies at Van Hove singularities in the joint density of states can greatly enhance the SD effect, making it much larger than these estimates.

Optical activity research has attracted significant attention across several disciplines, including chemistry, material science, physics, and molecular biology. In recent years, research

\*oarteaga@ub.edu

on artificial optically active materials has been particularly remarkable [4]. However, spatial dispersion has received comparatively less attention. Most of the works in this area focus on studying the SD effects in metamaterials [5]. Possibly the most prominent effect of SD in a natural material became important in optical lithography in the far-UV [6]. Below a wavelength of 193 nm,  $\text{CaF}_2$  is almost the sole applicable material for refractive components [7]. Being a cubic crystal, it was first considered isotropic. However, when the industrial production of  $\text{CaF}_2$  crystals began, the first measurements of the birefringence at the target wavelength of 157 nm proved that  $\text{CaF}_2$  also shows birefringence stemming from spatial dispersion [8,9], which was far above the specifications for stress-induced birefringence. The SD for several cubic semiconductors such as GaAs [10], Ge [11], and Si [12] below the band gap was reported decades ago from transmission measurements that quantified the birefringence in single crystals.

Silicon, being the most widely used semiconductor material, plays a crucial role in numerous applications such as photovoltaic cells and microelectronics due to its unique optical properties. Furthermore, silicon is often used as a reference material in ellipsometry experiments due to the wide availability of high-quality wafers of crystalline silicon and the existence of extensive studies on its optical constants by various authors [13–16]. Traditionally, silicon has been considered a fully isotropic material with its permittivity reported as a scalar across the ultraviolet to infrared ranges, owing to its cubic crystal structure. However, silicon has a diamond cubic crystal lattice structure, which is a face-centered-cubic (fcc) arrangement of silicon atoms. The SD-induced anisotropy in silicon is primarily due to the orientation-dependent bond lengths and bond angles between neighboring silicon atoms in the crystal lattice, with crystallographic directions [100], [110], and [111] exhibiting different properties. For example, in terms of mechanical properties, the elastic constants, such as Young's modulus and Poisson's ratio, can vary with crystallographic direction [17]. Similarly, in terms of optical properties, the anisotropy of the crystal lattice can also result in different electromagnetic responses to the incident light. We believe this is most likely the reason why, in some works [18,19], slightly different optical constants have been reported from spectroscopic ellipsometry measurements depending on the crystal plane that was studied. The anisotropy of silicon was also detected from spectroscopic ellipsometry measurements by the group of Collins [20,21], although the effect was not attributed to SD.

This work employs Mueller matrix (MM) spectroscopic ellipsometry, a technique that measures the linear optical

response of samples or interfaces encoded in MM by analyzing the evolution of light reflected at the specular angle. MM ellipsometry is particularly suitable for characterizing anisotropic media, as standard ellipsometry may not capture cross-polarization phenomena that can arise in materials with an anisotropic optical response [22].

The organization of this work is as follows. First, we discuss the formal form for the permittivity tensor of silicon when SD is taken into account to analyze ellipsometry measurements with the Berreman  $4 \times 4$  formalism. Illustrative simulations are provided in Sec. II for two common orientations of single-crystal silicon wafers: (110) plane and (100) plane. MM ellipsometry experiments of light reflected on Si wafers at different angles of incidence (AOIs) and azimuths are described in Sec. III. Finally, Sec. IV provides the optical constants, including the effects of SD, that we have measured for silicon.

## II. DIELECTRIC TENSOR OF SPATIALLY DISPERSIVE SILICON

Silicon belongs to the cubic class  $m\bar{3}m$  or  $O_h$ , a centrosymmetric structure, and thus the second term in Eq. (1) vanishes. The SD tensor in Eq. (1) takes the same form as the elasto-optic tensor and thanks to invariance with respect to permutation of indices within the first ( $ij$ ) and second ( $ln$ ) pairs are usually presented as a  $6 \times 6$  matrix using Voigt notation. We denote this matrix as  $\alpha_{(ij)(ln)}$ , where indices grouped in parentheses, e.g., ( $ij$ ), would represent one single index in Voigt notation under the equivalences (11)  $\rightarrow$  1, (22)  $\rightarrow$  2, (33)  $\rightarrow$  3, (23) = (32)  $\rightarrow$  4, (31) = (13)  $\rightarrow$  5, and (21) = (12)  $\rightarrow$  6. For the cubic class  $m\bar{3}m$ , it takes the following matrix form:

$$\alpha_{(ij)(ln)} = \begin{pmatrix} \alpha_{11} & \alpha_{12} & \alpha_{12} & 0 & 0 & 0 \\ \alpha_{12} & \alpha_{11} & \alpha_{12} & 0 & 0 & 0 \\ \alpha_{12} & \alpha_{12} & \alpha_{11} & 0 & 0 & 0 \\ 0 & 0 & 0 & \alpha_{44} & 0 & 0 \\ 0 & 0 & 0 & 0 & \alpha_{44} & 0 \\ 0 & 0 & 0 & 0 & 0 & \alpha_{44} \end{pmatrix}. \quad (2)$$

Equation (1) can be directly used in infinite media, but not in calculations for layered media, which are the required ones for ellipsometry measurements [3]. Following the method in [3], it is possible to separate the electric and magnetic contributions in the expansion of the SD dispersion term in Eq. (1). The effective electric SD tensor  $\alpha_e$ , calculated by subtracting the effective magnetic SD contribution to the tensor, is given by

$$\alpha_{e(ik)(ln)} = \begin{pmatrix} \alpha_{11} & \alpha_{12} + 2\alpha_{44} & \alpha_{12} + 2\alpha_{44} & 0 & 0 & 0 \\ \alpha_{12} + 2\alpha_{44} & \alpha_{11} & \alpha_{12} + 2\alpha_{44} & 0 & 0 & 0 \\ \alpha_{12} + 2\alpha_{44} & \alpha_{12} + 2\alpha_{44} & \alpha_{11} & 0 & 0 & 0 \\ 0 & 0 & 0 & 0 & 0 & 0 \\ 0 & 0 & 0 & 0 & 0 & 0 \\ 0 & 0 & 0 & 0 & 0 & 0 \end{pmatrix}, \quad (3)$$

whereas the effect of magnetic contribution is a simple offset of the inverse permeability,  $\mu^{-1} = 1 + 2\alpha_{44}$ . Once the electric and magnetic contributions are decoupled and the optical activity term is omitted, the permittivity in Eq. (1) can be

redefined as

$$\varepsilon'_{(ij)}(\mathbf{m}) = \varepsilon^0_{(ij)} + \varepsilon^{SD}_{(ij)} = \varepsilon^0_{(ij)} + \alpha_{e(ij)(ln)} m_l m_n. \quad (4)$$

The term  $\varepsilon^0_{(ij)}$  is the permittivity tensor in absence of SD, while the term  $\varepsilon^{SD}_{(ij)}$  accounts for the contribution of electric SD.  $\mathbf{m}$  is the refraction vector:  $\mathbf{m} = (m_1 \ m_2 \ m_3)^T = n(c_1 \ c_2 \ c_3)^T$ , where  $n$  is the complex refractive index and  $c_i$  are the direction cosines of the wave vector.  $m$ , the modulus of the refraction vector, coincides with the refractive index:  $m^2 = m_1^2 + m_2^2 + m_3^2 = n^2$ .

If the components of  $\varepsilon^{SD}_{(ij)}$  are cast in a vector, they can be calculated from the following matrix-vector multiplication:

$$\begin{pmatrix} \varepsilon^{SD}_{11} \\ \varepsilon^{SD}_{22} \\ \varepsilon^{SD}_{33} \\ \varepsilon^{SD}_{23} \\ \varepsilon^{SD}_{13} \\ \varepsilon^{SD}_{12} \end{pmatrix} = \begin{pmatrix} \alpha_{11} & \alpha_{12} + 2\alpha_{44} & \alpha_{12} + 2\alpha_{44} & 0 & 0 & 0 \\ \alpha_{12} + 2\alpha_{44} & \alpha_{11} & \alpha_{12} + 2\alpha_{44} & 0 & 0 & 0 \\ \alpha_{12} + 2\alpha_{44} & \alpha_{12} + 2\alpha_{44} & \alpha_{11} & 0 & 0 & 0 \\ 0 & 0 & 0 & 0 & 0 & 0 \\ 0 & 0 & 0 & 0 & 0 & 0 \\ 0 & 0 & 0 & 0 & 0 & 0 \end{pmatrix} \begin{pmatrix} m_1^2 \\ m_2^2 \\ m_3^2 \\ 2m_2m_3 \\ 2m_1m_3 \\ 2m_1m_2 \end{pmatrix}. \quad (5)$$

Therefore, the following nonvanishing terms are obtained:

$$\varepsilon^{SD}_{11} = \alpha_{11}m_1^2 + (\alpha_{12} + 2\alpha_{44})(m_2^2 + m_3^2) = (\alpha_{12} + 2\alpha_{44})n^2 + (\alpha_{11} - \alpha_{12} - 2\alpha_{44})m_1^2, \quad (6a)$$

$$\varepsilon^{SD}_{22} = \alpha_{11}m_2^2 + (\alpha_{12} + 2\alpha_{44})(m_1^2 + m_3^2) = (\alpha_{12} + 2\alpha_{44})n^2 + (\alpha_{11} - \alpha_{12} - 2\alpha_{44})m_2^2, \quad (6b)$$

$$\varepsilon^{SD}_{33} = \alpha_{11}m_3^2 + (\alpha_{12} + 2\alpha_{44})(m_1^2 + m_2^2) = (\alpha_{12} + 2\alpha_{44})n^2 + (\alpha_{11} - \alpha_{12} - 2\alpha_{44})m_3^2. \quad (6c)$$

In the above results, it is evident that SD also generates an “isotropic” contribution to all  $\varepsilon^{SD}_{(ij)}$  components that is wave-vector independent [it is produced by the term  $(\alpha_{12} + 2\alpha_{44})n^2$  in Eqs. (6)]. As this term is, in practice, fully indistinguishable from  $\varepsilon^0_{(ij)}$  both from transmission or reflection measurements, we may reorganize Eq. (4) as

$$\begin{aligned} \boldsymbol{\varepsilon}(\mathbf{m}) &= \varepsilon \mathbf{I} + \begin{pmatrix} p_1 m_1^2 & 0 & 0 \\ 0 & p_1 m_2^2 & 0 \\ 0 & 0 & p_1 m_3^2 \end{pmatrix} \\ &\simeq \varepsilon \mathbf{I} + \varepsilon p_1 \begin{pmatrix} c_1^2 & 0 & 0 \\ 0 & c_2^2 & 0 \\ 0 & 0 & c_3^2 \end{pmatrix}, \end{aligned} \quad (7)$$

where  $\mathbf{I}$  is the  $3 \times 3$  identity matrix,  $\varepsilon \equiv \varepsilon^0 + (\alpha_{12} + 2\alpha_{44})n^2 \simeq \varepsilon^0(1 + \alpha_{12} + 2\alpha_{44})$ , and  $p_1 \equiv \alpha_{11} - \alpha_{12} - 2\alpha_{44}$ . However, due to  $\mu^{-1} = 1 + 2\alpha_{44}$ ,  $\mu^{-1}$  and  $\varepsilon$  cannot be disentangled from fits of our experimental data, being both offset by the same quantity  $2\alpha_{44}$  and independent of the wave-vector direction. In all fits, we therefore set  $\mu^{-1} = 1$ , in agreement with Si being nonmagnetic, even though exhibiting SD. With this parametrization,  $\varepsilon$  and  $p_1$  are the two experimentally measurable parameters that define the permittivity tensor of silicon. Specifically,  $\varepsilon$  represents the part of the permittivity that is not affected by the direction of the wave vector or, in other words, is unaffected by the crystal cut for a given wave vector. On the other hand,  $p_1$  represents the part of the permittivity that depends on the direction of the wave vector. It could be stated that  $\varepsilon$  is the dielectric tensor usually reported in the literature, but this is only “approximately” true, as the lack of consideration of SD in previous studies does not necessarily imply that the reported values of the dielectric constant were, in all cases, unaffected by SD.

Next, we describe how the tensor  $\boldsymbol{\varepsilon}(\mathbf{m})$  can be incorporated into Berreman’s matrix formalism [23] to model the experimental optical response in the presence of SD. With the usual description of Berreman’s formalism where the direction of the stratification is along the positive  $z$  axis, the direction cosines of the wave vector *inside* the material are

$$\begin{bmatrix} c_1 \\ c_2 \\ c_3 \end{bmatrix} = \mathbf{S} \begin{bmatrix} 0 \\ \sin \theta \\ \cos \theta \end{bmatrix} = \mathbf{S} \frac{1}{\sqrt{\varepsilon}} \begin{bmatrix} 0 \\ \sin \theta_0 \\ \sqrt{\varepsilon - \sin^2 \theta_0} \end{bmatrix}, \quad (8)$$

where  $\theta$  is the complex refraction angle and  $\theta_0$  is the real angle of incidence (AOI) of the ellipsometry experiment. As SD is a small effect, Snell’s law can be applied without considering the impact that SD may have on the direction of the wave vector.  $\mathbf{S}$  is a  $3 \times 3$  matrix defining a three-dimensional (3D) rotation. It can be written as

$$\mathbf{S} = \mathbf{T}_{(abc)} \begin{bmatrix} \cos \phi & \sin \phi & 0 \\ -\sin \phi & \cos \phi & 0 \\ 0 & 0 & 1 \end{bmatrix}, \quad (9)$$

where  $\phi$  is the experimental azimuth angle (rotation about the sample surface normal) in the laboratory coordinate frame and  $\mathbf{T}_{(abc)}$  is given by the wafer cut. For the (100) and (110) planes,

$$\mathbf{T}_{(100)} = \mathbf{I}, \quad \mathbf{T}_{(110)} = \begin{bmatrix} -\frac{1}{\sqrt{2}} & 0 & \frac{1}{\sqrt{2}} \\ \frac{1}{\sqrt{2}} & 0 & \frac{1}{\sqrt{2}} \\ 0 & 1 & 0 \end{bmatrix}, \quad (10)$$

where  $\mathbf{T}_{(110)}$  is calculated from a 3D rotation with Euler angles  $180^\circ$ ,  $90^\circ$ , and  $45^\circ$  when given in the  $ZXZ$  order. This means that for the (110) wafer, the [001] crystal direction is parallel to the  $p$  polarization when  $\phi = 0^\circ$ . As a final step, to put the tensor in the laboratory reference frame, a transformation given by  $\mathbf{S}^T \boldsymbol{\varepsilon} \mathbf{S}$  must be applied to it.

TABLE I. Effective dielectric tensor in a cubic  $m3m$  crystal assuming  $\varepsilon = 14.5$  and  $p_1 = 0.1$  (these values have been chosen for illustration purposes only as realistic  $p_1$  values in silicon are complex and smaller) once applied to the crystallographic planes (110) and (100) for various  $\theta_0$  and  $\phi$ .

$\theta_0$	(110) wafer						(100) wafer					
	$\phi = 0^\circ$			$\phi = 45^\circ$			$\phi = 0^\circ$			$\phi = 45^\circ$		
$0^\circ$	15.23	0	0	14.86	0.36	0	14.5	0	0	14.50	0	0
	0	14.50	0	0.36	14.86	0	0	14.50	0	0	14.50	0
	0	0	15.23	0	0	15.23	0	0	15.95	0	0	15.95
$70^\circ$	15.18	0	0	14.87	0.33	0.17	14.50	0	0	14.54	0	0
	0	14.58	0	0.33	14.87	0.17	0	14.59	0	0	14.54	0
	0	0	15.18	0.17	0.17	15.20	0	0	15.86	0	0	15.86

After these calculations, the following symmetric tensor is obtained for the (100) plane:

$$\boldsymbol{\varepsilon}_{(100)} = \varepsilon \mathbf{I} + \varepsilon p_1 \begin{bmatrix} \sin^2(\phi)(c_2^2 - c_1^2) + c_1^2 & \frac{\sin(2\phi)(c_1^2 - c_2^2)}{2} & 0 \\ \frac{\sin(2\phi)(c_1^2 - c_2^2)}{2} & \sin^2(\phi)(c_1^2 - c_2^2) + c_2^2 & 0 \\ 0 & 0 & c_3^2 \end{bmatrix}, \quad (11)$$

where  $c_1 = \sin \theta_0 \sin \phi / \sqrt{\varepsilon}$ ,  $c_2 = \sin \theta_0 \cos \phi / \sqrt{\varepsilon}$  and  $c_3 = \sqrt{\varepsilon - \sin^2 \theta_0} / \sqrt{\varepsilon}$ ; while for the (110) plane,

$$\boldsymbol{\varepsilon}_{(110)} = \varepsilon \mathbf{I} + \frac{\varepsilon p_1}{2} \begin{bmatrix} \cos^2(\phi)(c_1^2 + c_2^2 - 2c_3^2) + 2c_3^2 & \frac{\sin(2\phi)(c_1^2 + c_2^2 - 2c_3^2)}{2} & -\cos(\phi)(c_1^2 - c_2^2) \\ \frac{\sin(2\phi)(c_1^2 + c_2^2 - 2c_3^2)}{2} & \sin^2(\phi)(c_1^2 + c_2^2 - 2c_3^2) + 2c_3^2 & -\sin(\phi)(c_1^2 - c_2^2) \\ -\cos(\phi)(c_1^2 - c_2^2) & -\sin(\phi)(c_1^2 - c_2^2) & c_1^2 + c_2^2 \end{bmatrix}, \quad (12)$$

where  $c_1 = (\sqrt{\varepsilon - \sin^2 \theta_0} - \sin \theta_0 \sin \phi) / \sqrt{2\varepsilon}$ ,  $c_2 = (\sqrt{\varepsilon - \sin^2 \theta_0} + \sin \theta_0 \sin \phi) / \sqrt{2\varepsilon}$ , and  $c_3 = \cos \phi \sin \theta_0 / \sqrt{\varepsilon}$ .

Table I presents a comparison of the effective dielectric tensor for crystallographic planes (110) and (100) of silicon, assuming real-only optical constants  $\varepsilon = 14.5$  and  $p_1 = 0.1$ . At normal incidence ( $\theta_0 = 0^\circ$ ), the (100) plane shows no anisotropy as  $\varepsilon_{11} = \varepsilon_{22}$ , while the (110) plane exhibits clear in-plane anisotropy, with the tensor changing with azimuthal rotation  $\phi$ . At oblique incidence ( $\theta_0 = 70^\circ$ ), the in-plane anisotropy of the (100) plane is negligible, but the out-of-plane response is anisotropic with  $\varepsilon_{11} \simeq \varepsilon_{22} \neq \varepsilon_{33}$ . This response can be linked to that of a uniaxial crystal with the optic axis perpendicular to the surface. However, the (110) plane still retains strong in-plane anisotropy even at oblique incidence.

In an ellipsometry experiment, the presence of SD in silicon will be detectable only if the measured data cannot be explained by a fully isotropic model within the experimental error. Therefore, prior to discussing the experimental measurements, it is important to assess how the redefined dielectric tensor for the (100) plane, given by Eq. (11), and the (110) plane, given by Eq. (12), may impact MM ellipsometry measurements. Using the Berreman formalism, we simulate the Mueller matrices corresponding to a hypothetical medium with SD (for this simulation, we have assumed  $\varepsilon = 14.5 + 1i$  and  $p_1 = 0.1 + 0.1i$  at the wavelength of  $\lambda = 660$  nm) studied as a function of the azimuth  $\phi$  and the AOI  $\theta_0$  [ $\mathbf{M}_{\text{SD}}^{\text{Sim}}(\theta_0, \phi)$ ]. Next, we check how well those simulations can be fit by a simpler model in which SD is neglected (i.e.,  $p_1 = 0$ ) and only  $\varepsilon$

is fitted, generating  $\mathbf{M}_{\text{NoSD}}^{\text{Fit}}(\theta_0)$ . We quantify the difference as

$$D = \|\mathbf{M}_{\text{SD}}^{\text{Sim}}(\theta_0, \phi) - \mathbf{M}_{\text{NoSD}}^{\text{Fit}}(\theta_0)\|_F, \quad (13)$$

where  $\|\cdot\|_F$  denotes the Frobenius norm.  $\mathbf{M}_{\text{NoSD}}^{\text{Fit}}(\theta_0)$  is always a block-diagonal Mueller matrix (or  $\Psi - \Delta$  matrix), but  $\mathbf{M}_{\text{SD}}^{\text{Sim}}(\theta_0, \phi)$  not necessarily. In general, larger values of  $D$  are better for the determination of SD since they imply that the experiments cannot be explained by an isotropic permittivity tensor. Values of  $D$  smaller than the experimental resolution indicate SD becoming undetectable.

For each plane, we calculate  $D$  for two types of simulations:

- (i) Setting the azimuth at  $0^\circ$  and varying the AOI between  $0^\circ$  and  $89^\circ$ .
- (ii) Fixing the AOI at  $70^\circ$  and varying the azimuth from  $0^\circ$  to  $180^\circ$ .

The calculated values of  $D$  are depicted in Fig. 1. For the (110) plane,  $D$  exhibits values up to 0.03 in both variable AOI measurements [Fig. 1(a)] and variable azimuth measurements [Fig. 1(b)]. However, variable azimuth measurements are advantageous for determining SD compared to variable AOI measurements, as the latter can result in an incidental fit at a specific AOI, where  $D$  does not exceed 0.01 within the experimentally available angles of incidence ( $50^\circ$  and  $80^\circ$ ). Figure 1(a) indicates that normal incidence is a favorable configuration for detecting SD in a (110) wafer, which is why some studies employing the reflection anisotropy spectroscopy (RAS) technique have reported anisotropic readings on (110) Si wafers attributed to surface anisotropy effects



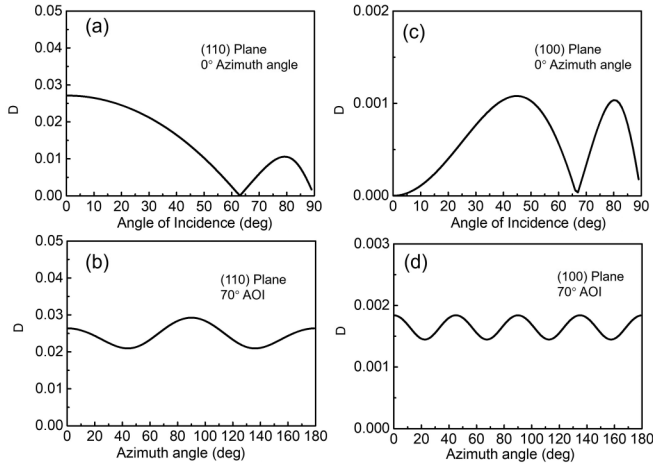


FIG. 1. Calculated  $D$  values for different simulation conditions: (a) (110) plane at 0° azimuth angle over AOIs from 0° to 89°; (b) (110) wafer at 70° AOI over azimuths from 0° to 180°; (c) (100) plane at 0° azimuth angle over AOIs from 0° to 89°; (d) (100) plane at 70° AOI over azimuths from 0° to 180°.

rather than SD [13,19,24,25]. When SD is disregarded, the best-fit values for Figs. 1(a) and 1(b) are  $\varepsilon_{NoSD} = 14.80 + 1.34i$  and  $\varepsilon_{NoSD} = 15.24 + 0.89i$ , respectively, which substantially differ from the  $\varepsilon$  value used in the simulation.

In the case of the (001) plane, the  $D$  values are consistently less than 0.002, which is more than an order of magnitude smaller than those of the (110) plane using the same optical constants. This indicates that this wafer cut is much less favorable for the determination of SD, as its optical response is much closer to the fully isotropic model. Another difference is that the plot of the variation of AOI [Fig. 1(c)] shows that the (001) wafer exhibits no anisotropy at normal incidence, as anticipated in Table I, indicating that only at oblique incidence is there some contribution from SD. As the anisotropy in the (001) wafer is out of plane, one would expect that measurements with varying AOI (particularly grazing angle measurements) would be most favorable for sensing SD; however, the large value of  $\varepsilon$  causes the wave-vector direction inside the crystal to always be close to the normal direction, thereby reducing sensitivity to the out-of-plane component. When SD is disregarded, the best-fit values for Figs. 1(c) and 1(d) are, respectively,  $\varepsilon_{NoSD} = 14.39 + 0.91i$  and  $\varepsilon_{NoSD} = 14.42 + 0.94i$ , which differ only slightly from the  $\varepsilon$  value used in the simulation.

Based on the obtained results, our approach for determining SD in silicon involved performing spectroscopic measurements at different azimuthal angles for a (110) Si wafer. Additionally, we conducted measurements on a (100) wafer to investigate if SD can also be detected in this crystal cut, despite our previous simulations showing that the SD effect in this wafer is more than 10 times smaller. In the case of the (100) wafer, the analysis was performed at variable AOI.

### III. EXPERIMENTS

The wafers investigated in this study are double-sided polished silicon wafers with (110) and (100) plane orientations, provided by Photon Export and Si-Mat companies,

respectively. For the ellipsometry measurements, we utilized a home-built four-photoelastic modulator (4PEM) Mueller matrix (MM) ellipsometer with a sensitivity better than 0.0005 in all MM elements, operating in the spectral range from 200 to 800 nm [26,27]. SD measurements are challenging due to their small effect, but the sensitivity of our system was generally sufficient. Perhaps the most challenging task was maintaining proper sample alignment during azimuthal rotation or changing the AOI, as even minor misalignments could affect MM values and potentially mask the effects of spatial dispersion.

The (110) silicon wafer was measured at an AOI of 70° with azimuthal angles ranging from 0° to 180°, with 15° intervals. Figure 2 displays the measurements at 0°, 45°, 90°, and 135° azimuthal angles. It is evident that SD affects not only the block-diagonal elements of the Mueller matrix, but also causes significant deviations from zero in the off-block diagonal elements at  $\phi = 45^\circ$  and  $135^\circ$  in the UV region, indicating cross polarization. To enhance visibility, the scale of the off-block-diagonal elements is magnified by a factor of 100.

In the case of (100) silicon, we initially attempted to investigate SD using an azimuthal rotation of the wafer, i.e., the same approach used for (110) silicon in Fig. 2. In the (100) plane, the MM is strictly block diagonal with no cross-polarizing elements at every 45° azimuthal angle ( $\phi = 0^\circ, 45^\circ, 90^\circ, 135^\circ$ , etc.), but there may be slight cross-polarizing elements between these values (e.g., for  $\phi = 22.5^\circ, 67.5^\circ$ , etc.). However, setting azimuthal rotations to such angles did not yield any measurable deviation in the off-block-diagonal elements within the noise of our ellipsometer and its alignment capabilities. This is not unexpected, considering the very small in-plane anisotropy of this crystallographic plane (as shown in Table I) compared to the (110) plane. Therefore, we conducted measurements on the (100) wafer at fixed azimuthal angles while varying the AOI ( $\theta_0$ ). In Fig. 3, we present the MM results obtained when the (100) wafer was measured at AOIs of 60°, 70°, and 85°. In this case, the off-block-diagonal elements are also magnified by a factor of 100 for improved visualization.

### IV. ANALYSIS AND DISCUSSION

For the analysis of the experiments, we employed the Berreman formalism considering the dielectric tensors provided in Eq. (11) and Eq. (12) to model the optical response of the wafers. The unknowns were  $\varepsilon$  and  $p_1$ , and all the fits described in this section were performed wavelength by wavelength, without assuming any predefined dispersion function. We initiated the fitting process in the near-infrared (NIR) (800 nm) and progressively moved towards shorter wavelengths so that the initial guess of the fitting parameters at each new wavelength was based on the fit result of the previous wavelength. The azimuthal angle  $\phi$  (with an error of  $\pm 0.5^\circ$ ) and the AOI  $\theta_0$  (with an error of  $\pm 0.1^\circ$ ) were fixed at their nominal experimental values and were not included in the fitting process. The native  $\text{SiO}_2$  overlayer, typically present on Si wafers, was taken into account by performing a preliminary fit limited to wavelengths above 500 nm, where SD is expected to have a negligible effect in reflection, using the

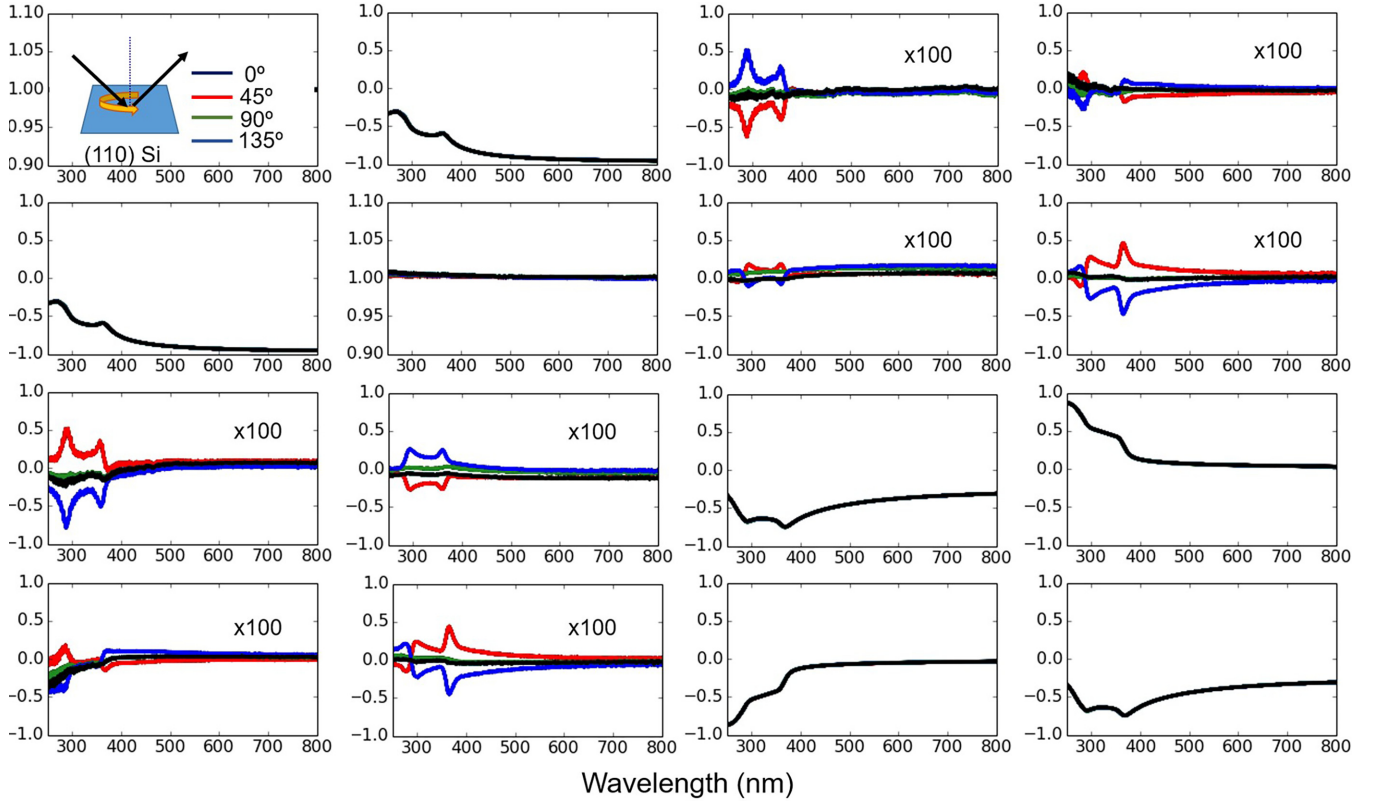


FIG. 2. MM of (110) silicon measured at  $70^\circ$  AOI, at the azimuth angles over wavelengths from 200 to 800 nm. The off-diagonal elements are magnified by 100.

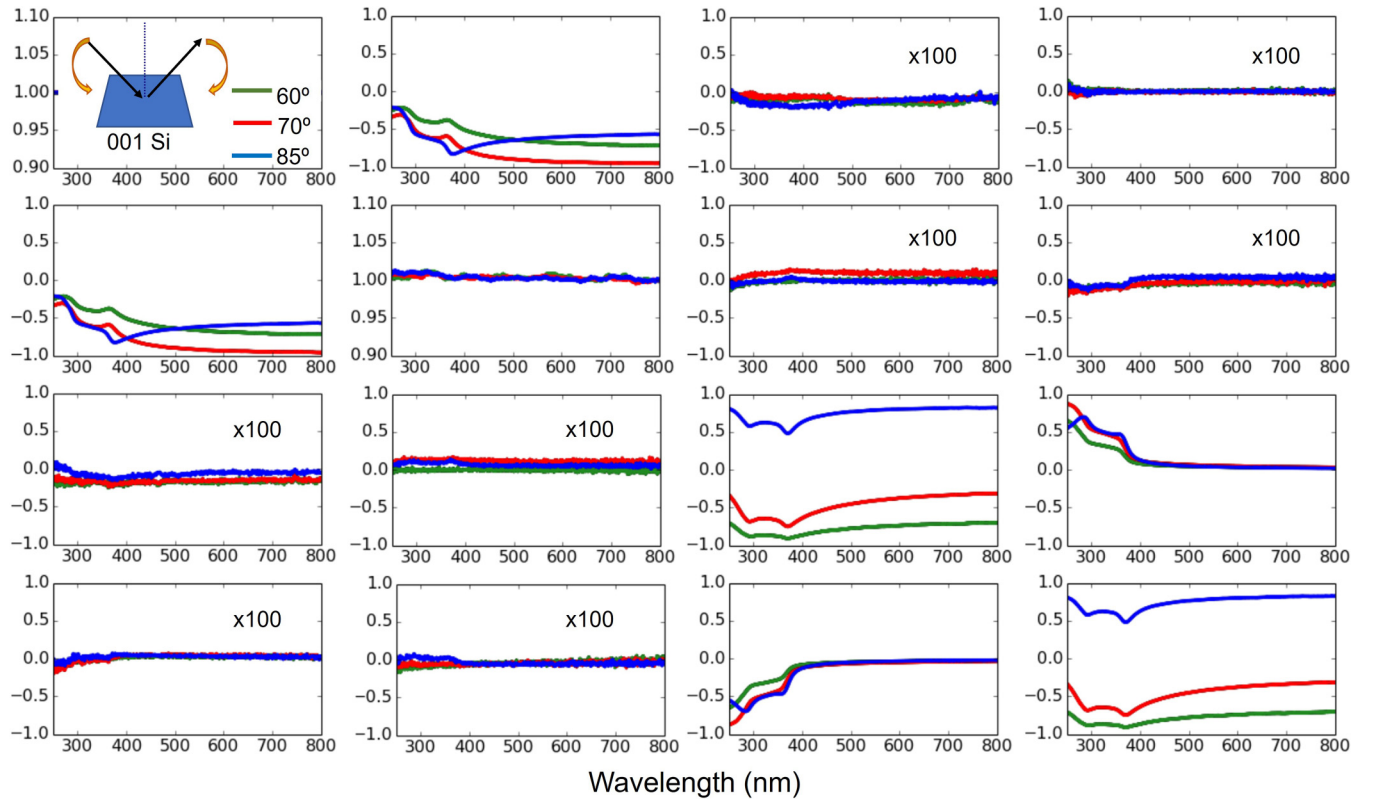


FIG. 3. Spectroscopic MM of (100) silicon ( $\phi = 0$ ), over AOIs from  $60^\circ$  to  $85^\circ$ . The off-block-diagonal elements are magnified by 100 to improve the visualization.

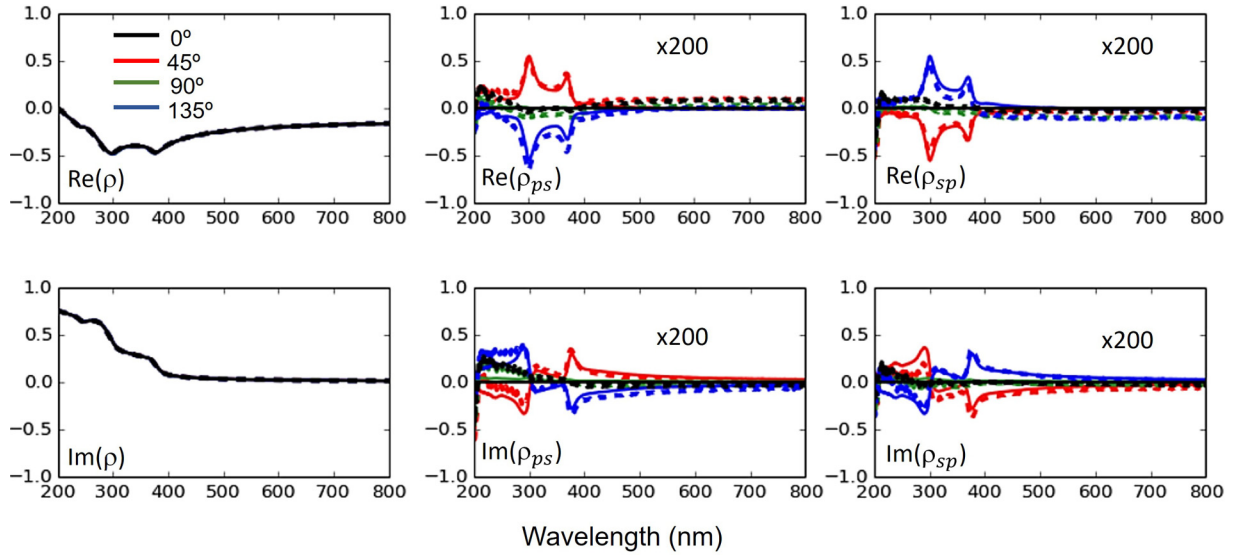


FIG. 4. Jones matrix elements corresponding to the MM given in Fig. 2. Experimental data (dashed line) and best fits (solid line) of (110) plane at 70° AOI over the azimuth angle from 0° to 180°. The scale of  $\rho_{ps}$  and  $\rho_{sp}$  is magnified by 200.

optical constants of silicon determined by Jellison [18]. The thickness of the overlayer was determined to be  $2.71 \pm 0.05$  nm for the (110) wafer and  $2.32 \pm 0.05$  nm for the (100) wafer. It should be noted that the variation of the thickness of the overlayer and AOIs has a subtle but non-negligible impact on the magnitude of  $p_1$ , but without influencing the position of the peaks. As measurements were always performed on wafers with the native oxide overlayer, the likely small role of surface-only contributions from chemisorbed and physisorbed species [24] was not studied in this work.

#### A. (110) wafer

$\varepsilon_{(110)}$  from Eq. (12) was fitted from the experimental data at variable azimuth. The formalism used generates a nondepolarizing Mueller matrix which can be equivalently expressed as a Jones matrix. Therefore, for ease of visualization, the experimental MMs in Fig. 2, which were completely nondepolarizing, have been transformed into normalized Jones matrices and compared with the fitting results in Fig. 4. The weak cross-polarization terms  $\rho_{ps}$  and  $\rho_{sp}$  that result from SD were accurately captured.

From this fit, the real and imaginary parts of  $\varepsilon$  were extracted and are displayed in Fig. 5(a). For comparison, we also executed an additional fit with only one fitting parameter,  $\varepsilon_{NoSD}$ , fully disregarding SD. Although, in the full scale of Fig. 5(a),  $\varepsilon$  and  $\varepsilon_{NoSD}$  seem to overlap, upon calculating their difference, there is a clear difference between them that is highly wavelength dependent, as shown in Fig. 5(b). In Fig. 5(c), the real and imaginary parts of  $p_1$  are presented, which take smaller values (below 0.1) compared to the scale of  $\varepsilon$ . Above 500 nm, the value of  $p_1$  is vanishingly small. The reduced  $\chi^2$  error function of the wavelength-by-wavelength fits is shown in Fig. 5(d). Clearly, without considering the SD dispersion term, it is not possible to get a good fit of the measurements in the UV region. However, for wavelengths above  $\sim 500$  nm, it is not necessary to include SD to get a good fit. This is indicative that above this wavelength, SD

effects essentially become smaller than the overall sensitivity of our ellipsometer, and therefore they have no influence on our experimental measurements.

In our wavelength-by-wavelength fittings, we leverage experimental data collected at many azimuth angles  $\phi$  to enhance the resilience and accuracy of our fits. However, it is worth noticing that a single spectroscopic MM measurement taken at an appropriate azimuth angle where the MM is not block diagonal (e.g.,  $\phi = 45^\circ$ ) suffices for the simultaneous determination of the real and imaginary components of both  $\varepsilon$  and  $p_1$ .

The largest values of SD that we have obtained are in the critical points near 3.4 and 4.2 eV, where  $p_1$  reaches values around 0.06. This is orders of magnitude larger than the values previously reported from transmission measurements below the band gap, where the birefringence [ $\Delta n = \sqrt{\varepsilon(1 + \frac{p_1}{2})} - \sqrt{\varepsilon}$ ] of silicon has been reported to be of the order of  $10^{-6}$  [12]. These very small values can still be measured from transmission measurements because  $\Delta n$  is amplified by the large factor resulting from  $2\pi l/\lambda$ , where  $l$  is the path length or thickness of the crystal and  $\lambda$  is the wavelength.

#### B. (100) wafer

The MM measured for the (100) wafer (Fig. 3) exhibits a block-diagonal form, indicating that the corresponding off-diagonal elements of the Jones matrix are zero. Unlike the (110) wafer, it is not feasible to perform a simultaneous fitting of  $\varepsilon$  and  $p_1$  for this wafer orientation: during the least-squares fitting process, a strong coupling between  $\varepsilon$  and  $p_1$  consistently emerges. We attempted to tackle this issue by splitting the fitting into two steps. First, we fitted  $\varepsilon$  while setting  $p_1$  to zero. Subsequently, we held the  $\varepsilon$  values fixed and fitted only  $p_1$ . However, introducing  $p_1$  into the second fit resulted in a minimal improvement in the reduced  $\chi^2$ . Furthermore, the standard deviation errors associated with parameter  $p_1$  were much larger than those determined for the (110) plane), as

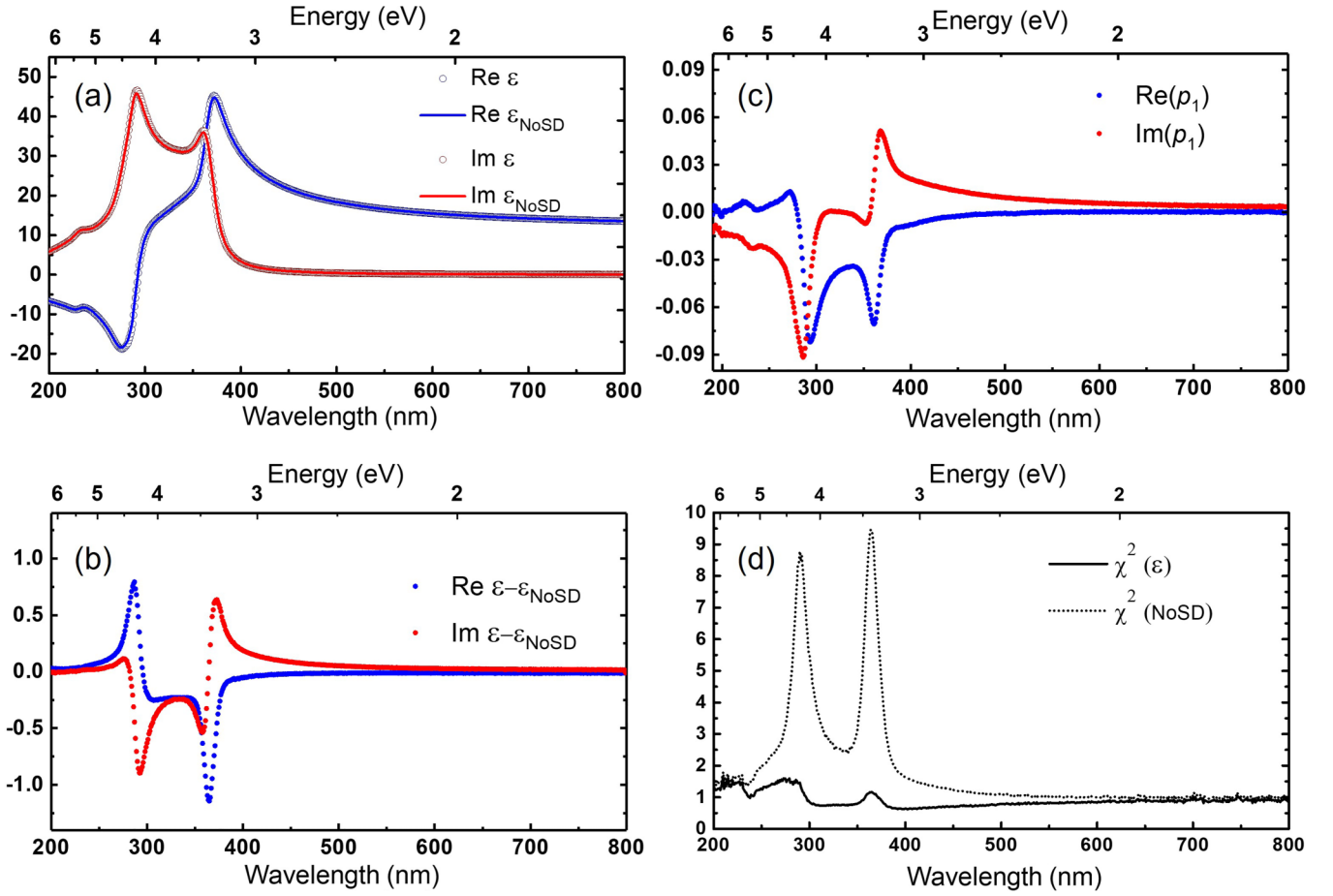


FIG. 5. Fit results of silicon (110). (a) Real and imaginary parts of the permittivity  $\epsilon$  values, i.e., one when considering spatial dispersion (dots) and the other when disregarding spatial dispersion (line)  $\epsilon_{\text{NoSD}}$ . (b) Difference between  $\epsilon$  and  $\epsilon_{\text{NoSD}}$ . (c) Real part and imaginary parts of  $p_1$ . (d)  $\chi^2$  of the fits with or without considering SD.

illustrated in Fig. 6. Consequently, we can conclude that the effects of SD on our experimental results for this crystallographic plane are virtually negligible within our experimental noise level and cannot be accurately quantified. This outcome is not surprising, as it aligns with our earlier simulations presented in Fig. 1, where the manifestation of SD in the (100)

plane was more than an order of magnitude smaller compared to the (110) plane.

### C. Comparison with literature values

In previous studies, the permittivity tensor of silicon has been reported from various crystallographic planes, revealing subtle but systematic deviations, particularly in the case of the (110) plane. However, in our analysis that takes into account SD, we found that the optical constants ( $n$  and  $k$ ) obtained from the (110) and (100) wafers show good agreement within our error levels. In Tables II and III, we respectively present a comparison between the  $n$  and  $k$  values obtained in this work and previous results from Jellison's work [18,28] as a reference. Notably, at UV wavelengths close to the critical points (e.g., 292 and 362 nm), the inclusion of SD effects in our study has resulted in an improved agreement between the  $n$  and  $k$  values obtained from the (110) and (100) wafers compared to previous works.

Another potential comparison lies in the relative reflectance difference of a (110) silicon wafer at near-normal incidence, investigated by Aspnes using the RAS technique [24]. Aspnes quantified the reflectance difference (RD) in a (110) Si wafer at near-normal incidence for light polarized along the directions  $[1\bar{1}0]$  and  $[001]$  of the crystal. The

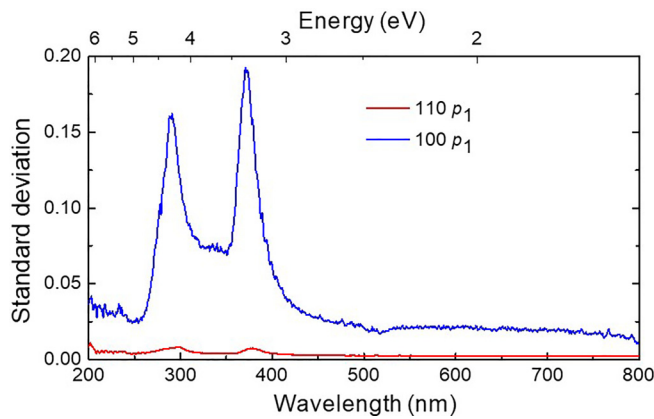


FIG. 6. Standard deviations of  $p_1$  extracted from (110) and (100) wafers (red and blue lines, respectively). The error in the determination from (100) is much larger than that from (110).



TABLE II. Comparison between selected values of the real ( $n$ ) part of the refractive index of (100) and (110) silicon from this work and those reported by Jellison in [28].

Wavelength (nm)	plane	$n$ (Ref. [28])	$n$ (this work)
248	100	$1.669 \pm 0.008$	$1.706 \pm 0.005$
248	110	$1.698 \pm 0.014$	$1.718 \pm 0.007$
292	100	$4.745 \pm 0.022$	$4.641 \pm 0.015$
292	110	$4.737 \pm 0.027$	$4.642 \pm 0.023$
362	100	$6.279 \pm 0.021$	$6.212 \pm 0.011$
362	110	$6.259 \pm 0.037$	$6.209 \pm 0.010$
400	100	$5.595 \pm 0.009$	$5.585 \pm 0.006$
400	110	$5.572 \pm 0.032$	$5.591 \pm 0.014$
450	100	$4.675 \pm 0.006$	$4.676 \pm 0.009$
450	110	$4.669 \pm 0.024$	$4.662 \pm 0.008$
515	100	$4.218 \pm 0.005$	$4.204 \pm 0.005$
515	110	$4.211 \pm 0.020$	$4.219 \pm 0.005$
635	100	$3.864 \pm 0.004$	$3.853 \pm 0.003$
635	110	$3.866 \pm 0.017$	$3.861 \pm 0.005$

experimental results he obtained are depicted in Fig. 7, alongside our calculated values derived from our previously determined  $\varepsilon$  and  $p_1$  complex values and also incorporating the native  $\text{SiO}_2$  overlayer in the calculus. These RD values at normal incidence can be readily calculated from Eq. (12) when both  $\theta$  and  $\phi$  are set to zero: in this scenario,  $\varepsilon_{(110)}$  is a diagonal tensor, and its first diagonal element can be utilized to compute the reflectivity for polarization along the [001] direction, while the second diagonal element can provide the reflectivity for polarization along the  $[1\bar{1}0]$  direction. The comparison in Fig. 7 demonstrates a strong correspondence between the experimental data obtained via the RAS technique and our results, indicating that spatial dispersion consistently accounts for the observed reflectance anisotropy values. Notably, spectroscopic ellipsometry offers an advantage over the RAS technique as it enables the simultaneous determination of the real and imaginary parts of both  $\varepsilon$  and  $p_1$ .

TABLE III. Comparison between selected values of the imaginary ( $k$ ) part of the refractive index of (100) and (110) silicon from this work and those reported by Jellison in [28].

Wavelength (nm)	Plane	$k$ (Ref. [28])	$k$ (this work)
248	100	$3.593 \pm 0.009$	$3.551 \pm 0.005$
248	110	$3.630 \pm 0.011$	$3.556 \pm 0.007$
292	100	$4.863 \pm 0.022$	$4.930 \pm 0.015$
292	110	$4.938 \pm 0.037$	$4.908 \pm 0.023$
362	100	$2.860 \pm 0.020$	$2.840 \pm 0.011$
362	110	$2.798 \pm 0.029$	$2.861 \pm 0.010$
400	100	$0.304 \pm 0.006$	$0.291 \pm 0.004$
400	110	$0.297 \pm 0.004$	$0.308 \pm 0.014$
450	100	$0.093 \pm 0.004$	$0.092 \pm 0.009$
450	110	$0.092 \pm 0.002$	$0.083 \pm 0.008$
515	100	$0.039 \pm 0.003$	$0.034 \pm 0.005$
515	110	$0.039 \pm 0.002$	$0.037 \pm 0.005$
635	100	$0.015 \pm 0.003$	$0.013 \pm 0.003$
635	110	$0.015 \pm 0.001$	$0.014 \pm 0.005$

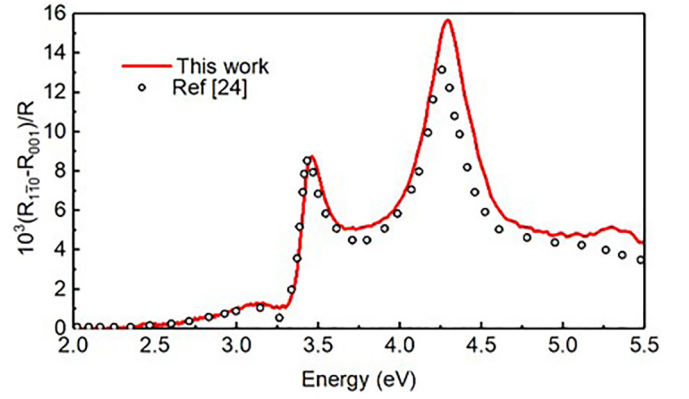


FIG. 7. Relative reflectance difference spectra for normal incidence light polarized along  $[1\bar{1}0]$  (reflectance  $R_{1\bar{1}0}$ ) and  $[001]$  (reflectance  $R_{001}$ ) in a naturally oxidized (110) Si surface.  $R$  is the average of these two reflectances. Black circles are experimental values from Ref. [24] and the red line is calculated from our measured values of  $\varepsilon$  and  $p_1$ .

Our results suggest that the anisotropy of the silicon's permittivity, as described by the parameter  $p_1$ , can influence various aspects of its electronic properties. It most likely has a translation into properties of the band structure, joint density of states, distribution of electronic bond charges, and charge transport properties along different crystallographic directions. Among these directions, the  $[110]$  direction (or other equivalent directions along the diagonals of the faces of the cubic fcc lattice) stands out as the most anisotropic in ellipsometry or polarimetry measurements. X-ray studies have also revealed a slight skewing or asymmetry of the electron cloud towards the  $[110]$  direction [29,30]. This deviation in the  $sp^3$  electronic states of the silicon atom, which we also attribute to SD, correlates with the relatively significant values of  $p_1$  observed at critical points. These findings suggest that the anisotropy of the crystal lattice can have a non-negligible impact on the electronic properties of silicon. However, the microscopic models that underlie this phenomenon and their implications on the band structure are beyond the scope of this study.

## V. SUMMARY

In this work, we present a complete experimental determination of the spectroscopic permittivity tensor of crystalline silicon when taking into account the SD effect. The tensor is described by two complex terms,  $\varepsilon$  and  $p_1$ , where  $p_1$  is the wave-vector-dependent term responsible for SD. We observe that in the UV region, the anisotropy of silicon is clearly visible from spectroscopic ellipsometry measurements on a (110) silicon wafer, indicating an effect up to five orders of magnitude larger than in the transparent NIR region, where spatial dispersion can only be observed from transmission measurements. Measurements of the (100) crystallographic plane showed a vanishing anisotropy effect, in agreement with the tensor form that we present. Our comparative analysis between (100) and (110) wafers indicates that once SD is taken into account, the values of  $\varepsilon$  obtained from the (100) and (110) planes are in good agreement. The measurement of

$p_1$  from spectroscopic ellipsometry measurements was only possible for (110) wafers.

### ACKNOWLEDGMENTS

This work was funded by the Ministerio de Ciencia Innovación y Universidades Grants No. RYC2018-024997-I

and No. TED2021-129639B-I00 (MCIU/AEI/FEDER, UE), China Scholarship Council (Grant No. 202108350066), National Natural Science Foundation of China (Grant No. 52275531), and European Metrology Programme for Innovation and Research Grant No. 20IND04ATMOC (10.13039/100014132).

- [1] V. M. Agranovich and V. Ginzburg, *Crystal Optics with Spatial Dispersion, and Excitons* (Springer Science & Business Media, New York, 2013), Vol. 42.
- [2] R. Ossikovski, O. Arteaga, and C. Sturm, Constitutive relations for optically active anisotropic media: A review, *Adv. Photon. Res.* **2**, 2100160 (2021).
- [3] R. Ossikovski and O. Arteaga, Optical response of media and structures exhibiting spatial dispersion, *Opt. Lett.* **47**, 5602 (2022).
- [4] Y. Liu and X. Zhang, Metamaterials: A new frontier of science and technology, *Chem. Soc. Rev.* **40**, 2494 (2011).
- [5] A. Poddubny, I. Iorsh, P. Belov, and Y. Kivshar, Hyperbolic metamaterials, *Nat. Photon.* **7**, 948 (2013).
- [6] A. G. Serebryakov and F. Bociort, Spatial dispersion of crystals as a critical problem for deep UV lithography, *J. Opt. Technol.* **70**, 566 (2003).
- [7] M. Letz, W. Mannstadt, M. Brinkmann, and E. Moersen, Spatial dispersion in  $\text{CaF}_2$  caused by the vicinity of an excitonic bound state, in *Optical Microlithography XV*, edited by A. Yen, International Society for Optics and Photonics (SPIE, Bellingham, WA, 2002), Vol. 4691, pp. 1761–1768.
- [8] J. H. Burnett, Z. H. Levine, and E. L. Shirley, Intrinsic birefringence in calcium fluoride and barium fluoride, *Phys. Rev. B* **64**, 241102(R) (2001).
- [9] J. H. Burnett, Z. H. Levine, E. L. Shirley, and J. H. Bruning, Symmetry of spatial-dispersion-induced birefringence and its implications for  $\text{CaF}_2$  ultraviolet optics, *J. Micro/Nanolith. MEMS MOEMS* **1**, 213 (2002).
- [10] Y. Y. Peter and M. Cardona, Spatial dispersion in the dielectric constant of GaAs, *Solid State Commun.* **9**, 1421 (1971).
- [11] P. Yu and M. Cardona, Spatial dispersion induced birefringence in cubic semiconductors, in *Computational Solid State Physics: Proceedings of an International Symposium Held October 6–8, 1971, Wildbad, Germany*, edited by F. Herman, N. W. Dalton, and T. R. Koehler (Springer, New York, 1972), pp. 7–21.
- [12] J. Pasternak and K. Veda, Optical anisotropy of silicon single crystals, *Phys. Rev. B* **3**, 2567 (1971).
- [13] D. E. Aspnes and A. A. Studna, Dielectric functions and optical parameters of Si, Ge, GaP, GaAs, GaSb, InP, InAs, and InSb from 1.5 to 6.0 eV, *Phys. Rev. B* **27**, 985 (1983).
- [14] C. Herzinger, B. Johs, W. McGahan, J. A. Woollam, and W. Paulson, Ellipsometric determination of optical constants for silicon and thermally grown silicon dioxide via a multi-sample, multi-wavelength, multi-angle investigation, *J. Appl. Phys.* **83**, 3323 (1998).
- [15] G. E. Jellison Jr. and F. Modine, Optical constants for silicon at 300 and 10 K determined from 1.64 to 4.73 eV by ellipsometry, *J. Appl. Phys.* **53**, 3745 (1982).
- [16] T. Nagashima and M. Hangyo, Measurement of complex optical constants of a highly doped Si wafer using terahertz ellipsometry, *Appl. Phys. Lett.* **79**, 3917 (2001).
- [17] J. Kim, D.-i. Cho, and R. S. Muller, Why is (111) silicon a better mechanical material for MEMS? in *Transducers 01 Euroensors XV: The 11th International Conference on Solid-State Sensors and Actuators June 10–14, 2001, Munich, Germany*, edited by E. Obermeier (Springer, New York, 2001), pp. 662–665.
- [18] G. E. Jellison Jr., Optical functions of silicon determined by two-channel polarization modulation ellipsometry, *Opt. Mater.* **1**, 41 (1992).
- [19] K. Bell, L. Mantese, U. Rossow, and D. Aspnes, Systematic differences among nominal reference dielectric function spectra for crystalline Si as determined by spectroscopic ellipsometry, *Thin Solid Films* **313-314**, 161 (1998).
- [20] C. Chen, I. An, and R. Collins, Multichannel Mueller matrix ellipsometry for simultaneous real-time measurement of bulk isotropic and surface anisotropic complex dielectric functions of semiconductors, *Phys. Rev. Lett.* **90**, 217402 (2003).
- [21] C. Chen, I. An, and R. Collins, Simultaneous determination of bulk isotropic and surface-induced anisotropic complex dielectric functions of semiconductors from high speed Mueller matrix ellipsometry, *Thin Solid Films* **455-456**, 196 (2004).
- [22] O. Arteaga, E. Garcia-Caurel, and R. Ossikovski, Anisotropy coefficients of a Mueller matrix, *J. Opt. Soc. Am. A* **28**, 548 (2011).
- [23] D. W. Berreman, Optics in stratified and anisotropic media:  $4 \times 4$ -matrix formulation, *J. Opt. Soc. Am.* **62**, 502 (1972).
- [24] D. E. Aspnes and A. A. Studna, Anisotropies in the above band-gap optical spectra of cubic semiconductors, *Phys. Rev. Lett.* **54**, 1956 (1985).
- [25] K. Bell, L. Mantese, U. Rossow, and D. Aspnes, Surface and interface effects on ellipsometric spectra of crystalline Si, *J. Vac. Sci. Technol. B* **15**, 1205 (1997).
- [26] O. Arteaga, J. Freudenthal, B. Wang, and B. Kahr, Mueller matrix polarimetry with four photoelastic modulators: Theory and calibration, *Appl. Opt.* **51**, 6805 (2012).
- [27] J. Gomis-Brescó and O. Arteaga, Use of complete temporal basis in polarimeters based on photoelastic modulators, *Opt. Lett.* **48**, 1966 (2023).
- [28] G. E. Jellison and P. C. Joshi, Crystalline silicon solar cells, in *Spectroscopic Ellipsometry for Photovoltaics: Fundamental Principles and Solar Cell Characterization*, edited by H. Fujiwara and R. W. Collins (Springer International, Cham, 2018), Vol. 1, pp. 201–225.
- [29] J. Roberto, B. Batterman, and D. Keating, Diffraction studies of the (222) reflection in Ge and Si: Anharmonicity and the bonding electron, *Phys. Rev. B* **9**, 2590 (1974).
- [30] J. Z. Tischler and B. W. Batterman, Determination of magnitude, phase, and temperature dependence of forbidden reflections in silicon and germanium, *Phys. Rev. B* **30**, 7060 (1984).